An efficient adaptive implicit scheme with equivalent continuum approach for two-phase flow in fractured vuggy porous media

Wang, Luyu; Golfier, Fabrice; Tinet, Anne-Julie; Chen, Weizhong; Vuik, Cornelis

**Citation (APA)**
Wang, L., Golfier, F., Tinet, A.-J., Chen, W., & Vuik, C. (2022). An efficient adaptive implicit scheme with equivalent continuum approach for two-phase flow in fractured vuggy porous media. *Advances in Water Resources*, *163*, 1-15. Article 104186. https://doi.org/10.1016/j.advwatres.2022.104186

**Important note**
To cite this publication, please use the final published version (if applicable).
Please check the document version above.

# An efficient adaptive implicit scheme with equivalent continuum approach for two-phase flow in fractured vuggy porous media

Luyu Wang [a,*], Fabrice Golfier [a], Anne-Julie Tinet [a], Weizhong Chen [c], Cornelis Vuik [b]

[a] *GeoRessources Lab., UMR 7359, CNRS, 54500 Vandœuvre-lès-Nancy, France*
[b] *Department of Applied Mathematics, Delft University of Technology, 2628 CD Delft, The Netherlands*
[c] *Institute of Rock and Soil Mechanics, Chinese Academy of Sciences, 430071 Wuhan, China*

## ARTICLE INFO

## ABSTRACT

This work investigates numerical method and equivalent continuum approach (ECA) of fluid flow in fractured porous media. The commonly used discrete fracture model (DFM) without upscaling needs full discretization of all fractures. It enjoys the merit of capturing each fracture accurately but will get in trouble with mesh partition and low computational efficiency, especially when a complex geometry is involved. In this study, we develop an efficient implicit scheme with adaptive iteration, in which an improved ECA is devised and then integrated in this scheme. Numerical studies show that the proposed numerical scheme improves the convergence condition and computational efficiency. Then, a test is conducted to demonstrate the feasibility of using superposition principle of permeability tensor in upscaling. Based on these, different strategies are applied to simulate fluid flow in fracture networks with a complex geometry. It is demonstrated that the proposed ECA is able to reproduce the results computed by DFM. The accuracy depends on resolution of background grids. The presented method enjoys a low computational cost and desirable convergence performance compared with the standard DFM in which equivalent continuum is not considered.

## 1. Introduction

Previous studies have revealed that the presence of discrete fractures has significant influence on characteristics of fractured porous media (Berkowitz, 2002; Adler et al., 2013; Wang et al., 2020). However, modeling of flow and transport in fractured porous media raises numerical challenges in geoscience applications (Cotta et al., 2020; Medici et al., 2021; Wang et al., 2022). In the community of geological modeling, there are two main categories of the computational model, namely the discrete fracture model (DFM) (Aliouache et al., 2019; Wang et al., 2022) and the equivalent continuum model (Kottwitz et al., 2021; Lasseux et al., 2021). This work intends to study the compromise between the accuracy of DFM and the convenience of equivalent continuum model. We focus on two-phase flow in fractured porous media, and discuss the extension to a more general case, namely fractured vuggy porous media, which has gained much attention in recent years (Yan et al., 2019; Mohammed et al., 2021; Xu et al., 2022).

There are two main groups of numerical method dealing with the interaction between fractures and matrix, namely conformal and non-conformal mesh schemes. The classical DFM is a widely used conformal mesh scheme. DFM was presented to explicitly reproduce

stochastic fractures based on field investigation. Normally, the fractures are simulated by the low-dimensional elements lying on the interface of matrix elements (Wang et al., 2022). It enjoys several merits, such as simulating each fracture accurately and a desirable flexibility to directly borrow the numerical discretizations from finite element and finite volume methods (Gläser et al., 2017; Wang et al., 2019, 2022). However, it may encounter some difficulties of complicated mesh strategy required by the conformal grids and an expensive cost if a complex geometry is considered (Bahrainian et al., 2015; Fourno et al., 2019; Xie and Edwards, 2021). Indeed, the presence of fractures and vugs may introduce a complex topology of the geometry, which reduces the quality of convergence condition, and then leads to unnecessary cost. To this end, the non-conformal mesh scheme and the equivalent continuum model were introduced as two representative methods to simplify the connection of fractures-matrix (Ţene et al., 2017; Azizmohammadi and Sedaghat, 2020; Lasseux et al., 2021). These methods try to find a balance and compromise between accuracy and efficiency, but none can be done without drawbacks. In the scope of non-conformal mesh, EDFM (Embedded DFM) is developed as an alternative version of traditional DFM (Zhang et al., 2017; Hajibeygi et al., 2020). In

---

the last decade, other non-conformal methods have been proposed, typically the extended finite element method (Ren et al., 2018), phase-field method (Lee et al., 2018) and Lagrangian multipliers (Schädle et al., 2019). A transfer function is introduced to capture the connection between the embedded fractures and the surrounding matrix. Nevertheless, accuracy of non-conformal mesh schemes is highly relying on the interpolation manners on fractures and the flux transfer function. It is a trade-off between accuracy and the complicated conformal meshing. In contrast, DFM-based methods allow directly employing the traditional numerical discretization schemes, such that the accuracy can be ensured (Gläser et al., 2017; Tan et al., 2021; Wang et al., 2022).

The hierarchical modeling technique, based on the concept of equivalent continuum model, was introduced to upscale small size fractures and retaining the relative larger size fractures (Lee et al., 2001; Yan et al., 2021; Lasseux et al., 2021). In this way, the computational efficiency improves a lot, but the accuracy highly depends on the grid resolution of the upscaled models. In general, the methods of calculating equivalent permeability tensor of the equivalent continuum model can be categorized into two main groups. The first group is based on the analytical methods pioneered by Snow (1969) and Oda (1985). Later, there are some other analytical methods have been developed, for instance, critical path analysis (Adeyemi et al., 2022), homogenization (Mezhoud et al., 2020) and effective medium theory (Hosseini et al., 2021). Their application is restricted due to limitations of implementation and simplified assumptions. The second group is flow-based upscaling by numerical simulation (Kottwitz et al., 2021; Lasseux et al., 2021). It has been widely used in reservoir engineering and geoscience applications. Its merit is to be applicable for complex geometry. The presented work is based on the second strategy.

Despite being vital importance, there are still some open issues needed to be addressed. One key point is the criterion of upscaling. Although the equivalent continuum model enjoys some conveniences in effortless meshing and acceptable computational cost (Azizmohammadi and Sedaghat, 2020; Kottwitz et al., 2021; Lasseux et al., 2021), it is sophisticated to determine which fractures should be upscaled or retained. Besides, the grid resolution of the upscaled sub-blocks has great impact on numerical simulation. Therefore, it is worthwhile to study the impact of resolution on accuracy. On the other hand, the expensive computation cost of the DFM reduces the efficiency of simulation, especially if the presence of multiple fractures is considered. To solve this, in this work, we combine the advantages of the accuracy of DFM and the efficiency of equivalent continuum model. An improved equivalent continuum approach is presented to reduce the complexity of fractured media. In addition, we introduce the superposition principle of equivalent permeability tensor and integrating it into the upscaling scheme. At this point, some researchers have developed the superposition principle in fractured media (Lei et al., 2015; Xu and Yang, 2020). However, their discussions are restricted to single-phase flow in fractures with regular patterns. Particularly, upscaling of two-phase flow in fracture-vuggy network is rarely studied in the existing literature (Golfier et al., 2015; Yan et al., 2019; Wang et al., 2022).

In this work, we investigate numerical method and equivalent continuum approach of fractured media. Modeling approach of fractured vuggy porous media and the fully upscaling strategy are presented. Section 2 provides the mathematical formulation of two-phase flow in fractured vuggy porous media. Section 3 presents an efficient implicit scheme with adaptive iteration based on the hybrid-dimensional modeling. Section 4 proposes an equivalent continuum approach as well as the treatment regarding upscaling of a complex geometry. A general form of the superposition principle is introduced to evaluate equivalent permeability tensor in the equivalent model. In Section 5, a series of numerical tests is conducted to study the performance of the proposed scheme.
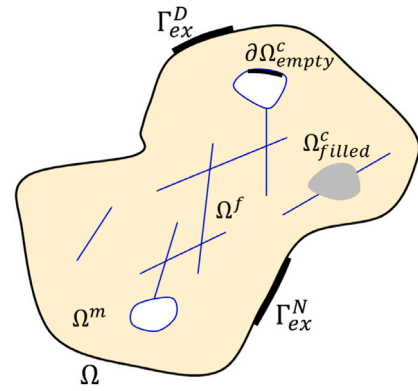


**Fig. 1.** Schematic of a fractured vuggy porous medium.

## 2. Mathematical model

In this section, formulation of the fractured media with complex geometrical structures is presented. A complex fractured medium is decomposed into several basic components. Then, the governing equations of two-phase flow in fractured media are given for completeness.

### 2.1. Physical domain of fractured vuggy porous media

Assuming a domain $\Omega$ consists of three sub-domains with the matrix $\Omega^m$, fractures $\Omega^f = \sum_i^{n_f} \Omega_i^f$ and cavities $\Omega^c = \sum_i^{n_c} \Omega_i^c$, as displayed in Fig. 1. The numbers of fracture and cavity distributed in this domain are $n_f$ and $n_c$, respectively.

Furthermore, $\Omega$ is confined by boundary $\Gamma$, including external and internal boundaries, denoted $\Gamma_{ex} = \Gamma_{ex}^N \cup \Gamma_{ex}^D$ and $\Gamma_{in} = \Gamma_{in}^N \cup \Gamma_{in}^D$. Note that the subscripts $N$ and $D$ are Neumann and Dirichlet types, respectively. Thus, the system of a porous medium containing stochastic cavities and fractures is defined as:

$$\Omega = \Omega^m \cup \Omega^f \cup \Omega^c, \quad \Gamma = \Gamma_{ex} \cup \Gamma_{in} \tag{1}$$

It is worth mentioning that the state of $\Omega^c$ can be varied, such as filled by geological materials $\Omega_{filled}^c$ or empty $\Omega_{empty}^c$. In the former case, the permeability of $\Omega_{filled}^c$ is allowed to be assigned to different values compared to the rock matrix $\Omega^m$. In the later case, $\Omega_{empty}^c$ is regarded as the sink or source. In this work, our approach allows the consideration of these states.

Hereafter, we will assume that the role of the empty cavity $\Omega_{empty}^c$ can be specified as an internal boundary $\Gamma_{in}$ imposed on the edge of it $\partial\Omega_{empty}^c$. If a Dirichlet type boundary condition, pressure $\bar{p}$, is applied, it reads:

$$p = \bar{p} \quad \text{on } \partial\Omega_{empty}^c \tag{2}$$

### 2.2. Governing equations for two-phase flow

The formulation for two incompressible and immiscible fluids in porous media is given as follows for completeness. The mass conservation for wetting phase $w$ and non-wetting phase $n$ is described by:

$$\frac{\partial (\phi S_\alpha)}{\partial t} + \nabla \cdot \mathbf{u}_\alpha = f_\alpha(S_\alpha) q, \quad \alpha = w, n \tag{3}$$

where $S_\alpha$ is saturation and $S_n + S_w = 1$. $\phi$ is porosity, $q$ volumetric flux. The frictional flow and phase velocity are represented by $f_\alpha(S_\alpha)$ and $\mathbf{u}_\alpha$, respectively. (Aziz, 1979; Hoteit and Firoozabadi, 2008).

The phase velocity is determined by Darcy's law (Pickup and Serbie, 1996; Kolditz et al., 2012). The relative permeability $k_{r\alpha}(S_\alpha)$ is involved as a function of $S_\alpha$:

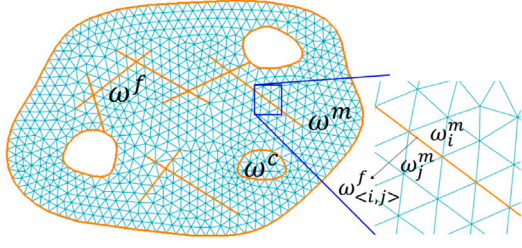$$\mathbf{u}_\alpha = -k_{r\alpha}(S_\alpha)\mu_\alpha^{-1}\mathbf{K}\nabla(p_\alpha - \rho_\alpha g Z), \quad \alpha = w, n \tag{4}$$

**Fig. 2.** Grids of a fractured vuggy porous medium.

where $\mathbf{K}$ is the absolute permeability tensor. $\mu_\alpha$ and $\rho_\alpha$ are the viscosity and density of phase $\alpha$. $g$ and $Z$ denote the gravity acceleration and depth, respectively. The two pressures are related by the capillary pressure $p_c(S_w) = p_n - p_w$. We refer to Hoteit and Firoozabadi (2008) for the detailed formulation.

For convenience, phase mobility $\lambda_\alpha(S_\alpha)$ is defined by $k_{r\alpha}(S_\alpha)\mu_\alpha^{-1}$. Total mobility is $\lambda_t = \lambda_w(S_w) + \lambda_n(S_n)$, therefore $f_\alpha(S_\alpha) = \lambda_\alpha(S_\alpha)/\lambda_t$. The total velocity is calculated by the summation of phase velocities:

$$\mathbf{u} = \mathbf{K}\left[-\lambda_t \nabla p_n + \lambda_w \nabla p_c + (\lambda_w \rho_w + \lambda_n \rho_n)g\nabla Z\right] \quad (5)$$

Initial and boundary conditions are required to confine the behavior on boundary and at the initial time $t_0$:

$$S_w = \bar{S}_w \quad \text{on } (\Omega^m \cup \Omega^f \cup \Omega^c) \times t_0$$
$$p_w = \bar{p} \quad \text{on } \Gamma_{ex}^D \times T_e \text{ or } \partial\Omega_{empty}^c \times T_e \quad (6)$$
$$-\lambda_t \mathbf{K}(\nabla p) \cdot \mathbf{n} = 0 \quad \text{on } \Gamma_{ex}^N \times T_e \text{ or } \partial\Omega_{empty}^c \times T_e$$

where $T_e = [t_0, t_n]$ is the entire time period, $\mathbf{n}$ the outward unit normal vector to $\Gamma$. $\bar{S}_w$ and $\bar{p}$ are the prescribed saturation and pressure, respectively. Combining Eqs. (3), (4) and (6), a well-posed system of partial differential equations (PDEs) is constructed to capture two-phase flow in a fractured vuggy porous medium.

## 3. Numerical method

In this section, the numerical method based on Galerkin finite element method is presented to discretize the governing equations Eqs. (3) and (5). An efficient implicit scheme with adaptive iteration is devised to efficiently solve the system of coupled PDEs.

### 3.1. Hybrid-dimensional mesh partition

The hybrid-dimensional elements are introduced to partition the fractures and matrix separately (Tan et al., 2021; Wang et al., 2022). We employed the commonly used conformal mesh, where fracture elements $\omega^f$ are lying along the edges of each pair of matrix elements $\omega^m$. As displayed in Fig. 2, an arbitrary pair of matrix elements is denoted by $< \omega_i^m, \omega_j^m >$. The intersection set operation of them is a fracture element lying between them, $\omega_i^m \cap \omega_j^m = \omega_{\langle i,j \rangle}^f$.

The open source software *Triangle* (Shewchuk, 2014) is used to generate grids on the matrix $\Omega^m = \cup_{i=1}^{n_e^m} \omega_i^m$ and cavities $\Omega^c = \cup_{i=1}^{n_e^c} \omega_i^c$. The filled and empty cavities are treated separately, and only filled cavities are meshed. Then, the fracture elements are generated based on the connectivity of the matrix and cavity cells, such that $\Omega^f = \cup_{i=1}^{n_e^f} \omega_i^f$. Numbers of the matrix, cavity and fracture elements are $n_e^m$, $n_e^c$ and $n_e^f$.

### 3.2. Formulation of the implicit scheme with adaptive iteration

To discretize the transport equation Eq. (3), the temporal integral is taken over a time increment $\Delta t$ and implicit difference scheme is used to discrete time-dependent term. For phase $\alpha$, it reads:

$$\underbrace{\int_\Omega \frac{\phi(\mathbf{x})}{\Delta t}\left(S_\alpha^{n+1} - S_\alpha^n\right) dV}_{\text{Time-dependent term}} + \underbrace{\int_\Omega \left[\nabla \cdot \mathbf{u}_\alpha\right]^{n+1} dV}_{\text{Flux term}} = \underbrace{\int_\Omega \left[f_\alpha(S_\alpha)q\right]^{n+1} dV}_{\text{Source term}} \quad (7)$$

The transport equation and Darcy's law construct a coupled system. The frictional velocity $\mathbf{u}_\alpha$ is obtained by the Darcy's law for multi-phase flow mentioned in Eq. (4). In implementation, it is commonly represented by the product $\mathbf{u}_\alpha = f_\alpha \mathbf{u}$, such that $f_\alpha$ is determined by the relative permeability $k_{r\alpha}(S_\alpha)$. Thereafter, $\mathbf{u}$ is directly represented by Eq. (5). We employ the implicit time discretization and substitute Eq. (5) into the following equation:

$$\int_\Omega -\nabla \cdot \mathbf{u}^{n+1} dV = \int_\Omega q^{n+1} dV \quad (8)$$

Eqs. (7) and (8) construct a coupled system of PDEs. We use Eq. (8) to calculate pressure. Then, the total velocity and frictional velocities can be obtained. The saturation is calculated from Eq. (7) based on the updated velocities.

According to the discussion in Section 3.1, the matrix and cavity elements are of higher-dimensional compared to fracture elements. Consequently, the residuals for each type are defined to solve the nonlinear system using implicit iterative scheme.

Following the notations defined in Section 3.1, for each $\omega_i^m$ or $\omega_i^c$, the residual is updated at each iterative step:

$$\left[R_i^{mc}\right]^{n+1} = -\frac{\phi(\mathbf{x})V_i^{mc}\xi_i}{\Delta t}\left(S_{\alpha,i}^{n+1} - S_{\alpha,i}^n\right) + \left[f_{\alpha,i}(S_{\alpha,i})q_i\right]^{n+1} V_i^{mc}$$
$$- \underbrace{\int_{\omega_i^{mc}} \left[\nabla \cdot \mathbf{u}_\alpha\right]^{n+1} dV}_{\text{Upwind term for } \omega_i^m \text{ or } \omega_i^c} \quad (9)$$

where $i = 1, \ldots, n_e^m$ or $n_e^c$. Note that $\omega_i^{mc}$ is either $\omega_i^m$ or $\omega_i^c$.

For each $\omega_i^f$, $i = 1, \ldots, n_e^f$, the residual is written as:

$$\left[R_i^f\right]^{n+1} = -\frac{\phi(\mathbf{x})L_i^f a_i^f \xi_i}{\Delta t}\left(S_{\alpha,i}^{n+1} - S_{\alpha,i}^n\right) + \left[f_{\alpha,i}(S_{\alpha,i})q_i\right]^{n+1} L_i^f a_i^f$$
$$- \underbrace{\int_{\omega_i^f} \left[\nabla \cdot \mathbf{u}_\alpha\right]^{n+1} dV}_{\text{Upwind term for } \omega_i^f} \quad (10)$$

where $\int_{\omega_i^*} \cdot$ represents an integral over the element. $V_i^{mc}$ is the volume of $\omega_i^m$ or $\omega_i^c$. $L_i^f$ and $a_i^f$ are length and aperture of $\omega_i^f$. The shape function $\xi$ equals 1 if a cell-centered scheme is applied. The third term in right hand side of above equations is determined by the upwind scheme respective to different elements. The expanded forms are given in Appendix A.

The iteration will be terminated once a criterion is satisfied, which is given by $\left\|\mathbf{R}^{n+1}\right\|_2 < \epsilon$. The tolerance $\epsilon$ is user defined, normally at a magnitude of $\sim 10^{-6}$. Usually, the time step $\Delta t$ is a fixed value defined in the input. However, this preference sometimes induces that the system has difficulty to converge and reduces computational efficiency.

To solve this issue, the adaptive iteration is devised to improve convergence condition, such that $\Delta t$ can be changed dynamically based on the condition of residual, as displayed in Fig. 3. Three values are introduced, $r_c$, $r_1$ and $r_2$. The new time increment, denoted by $\Delta t^*$, depends on the condition evaluated by the three values:

$$\Delta t^* = \begin{cases} r_1 \times \Delta t & \text{if } \left\|\mathbf{R}^{n+1}\right\|_2 < r_c \times \epsilon \\ r_2 \times \Delta t & \text{if } \left\|\mathbf{R}^{n+1}\right\|_2 > \epsilon \\ \Delta t & \text{otherwise} \end{cases} \quad (11)$$

Note that $0 < r_c < 1$, $0 < r_2 < 1$ and $r_1 > 1$. Eq. (11) is evaluated at the end of each iteration.

At each iteration, Eqs. (9) and (10) are calculated over all element until $i = n_e$, such that a residual vector is constructed $\mathbf{R} = [\mathbf{R}^m \quad \mathbf{R}^f \quad \mathbf{R}^c]^T$. Note that $n_e = n_e^m + n_e^c + n_e^f$. Then, Newton–Raphson approach is employed to obtain the updated saturation at each
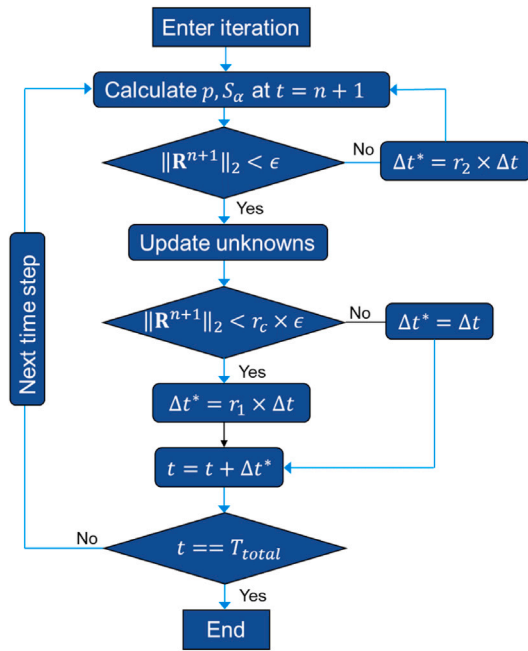
**Fig. 3.** Flowchart of the adaptive iteration.

iteration:

$$
\underbrace{\begin{bmatrix} \mathbf{J}^{mm} & \mathbf{J}^{mf} & \mathbf{J}^{mc} \\ \mathbf{J}^{fm} & \mathbf{J}^{ff} & \mathbf{J}^{fc} \\ \mathbf{J}^{cm} & \mathbf{J}^{cf} & \mathbf{J}^{cc} \end{bmatrix}}_{\mathbf{J}^{\nu}}^{\nu} \underbrace{\begin{bmatrix} \delta \mathbf{S}^m \\ \delta \mathbf{S}^f \\ \delta \mathbf{S}^c \end{bmatrix}^{\nu+1}}_{\delta \mathbf{S}^{\nu+1}} = - \underbrace{\begin{bmatrix} \mathbf{R}^m \\ \mathbf{R}^f \\ \mathbf{R}^c \end{bmatrix}^{\nu}}_{-\mathbf{R}^{\nu}}
\tag{12}
$$

where components of Jacobian $\mathbf{J}$ are calculated by $\mathbf{J} = \partial \mathbf{R} / \partial \mathbf{S}$ according to Eqs. (9) and (10). Note that the subscripts $m, f, c$ represent matrix, fracture and cavity. Consequently, the saturation in previous iteration $\mathbf{S}^{\nu}$ is updated by $\mathbf{S}^{\nu+1} = \mathbf{S}^{\nu} + \delta \mathbf{S}^{\nu+1}$. $\nu$ is the iterative number.

The high contrast of permeabilities on fractures and matrix would lead to an ill-conditioned Jacobian $\mathbf{J}$ with a high condition number, which would bring an inaccurate result. To this end, a preconditioning technique is proposed to better constrain the solution. The preconditioned Jacobian $\bar{\mathbf{J}}$ is derived by a preconditioner $\mathbf{P}$. Therefore, the expanded forms of $\mathbf{P}$ can be presented. It is easy to implement, which is given in Appendix B. The operation Eq. (B.1) provides an efficient and simple way to improve numerical quality of $\mathbf{J}$.

## 4. An equivalent continuum approach

In practice, the upscaling approach is usually used to simplify the complex fractured network and field heterogeneity. Consequently, the discrete fractures are upscaled into many sub-blocks with equivalent parameters. In this section, an equivalent continuum approach is devised based on the flow-based upscaling technique. Superposition principle is introduced to compute permeability tensor. Then, a treatment of complex geometries is addressed.

### 4.1. Upscaling for fluid flow in fractured porous media

The results of upscaling should be satisfied with the equation of the original problem. For convenience, the capillary pressure is assumed to be zero. Substituting the calculated solution into the original equation, it reads:

$$
q = -\nabla \cdot \left[ \mu^{-1} \widetilde{\mathbf{K}} \cdot (\nabla p^*) \right]
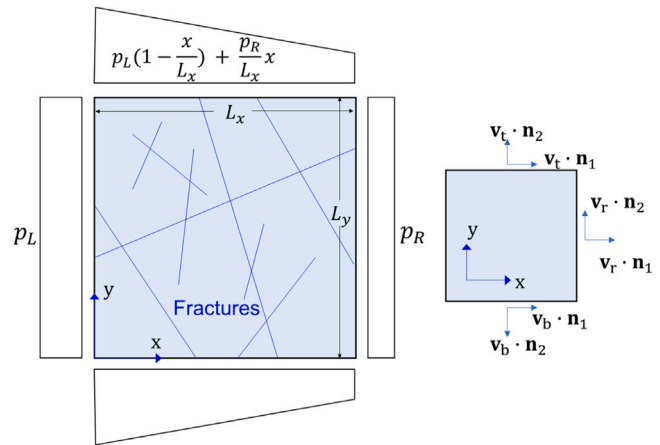\tag{13}
$$



**Fig. 4.** Boundary condition for calculating permeability tensor.

where $\widetilde{\mathbf{K}}$ is the equivalent permeability tensor. $p^*$ is the new solution calculated based on upscaled parameter. It means that $p^*$ should be close to the pressure in the original problem $p$ (Chen et al., 2015). The component form of $\widetilde{\mathbf{K}}$ is:

$$
\widetilde{\mathbf{K}} = \begin{bmatrix} \widetilde{k}_{xx} & \widetilde{k}_{xy} \\ \widetilde{k}_{yx} & \widetilde{k}_{yy} \end{bmatrix}
\tag{14}
$$

The expanded forms, given in Appendix C, are solved by the flow-based approach.

To calculate $\widetilde{k}_{xx}$ and $\widetilde{k}_{xy}$, as shown in Fig. 4, a pair of constant pressures, $p_L$ and $p_R$, are applied on the left and right hand sides, while the linear pressures $p_L(1 - x/L_x) + x p_R / L_x$ are applied on the top and bottom sides. Therefore, one can obtain the fluxes $q_x$ and $q_y$. Here, we use the calculation method proposed by Chen et al. (2015), in which the so-called multiple boundary upscaling is used to calculate the fluxes. If the inlet is placed on the left boundary (*l*), as illustrated in Fig. 4, we have:

$$
q_x^l = \int_{L_y} \mathbf{v}_r \cdot \mathbf{n}_1 \, dy + \int_{L_x} \mathbf{v}_t \cdot \mathbf{n}_1 \, dx + \int_{L_x} \mathbf{v}_b \cdot \mathbf{n}_1 \, dx
$$
$$
q_y^l = \int_{L_x} \mathbf{v}_t \cdot \mathbf{n}_2 \, dx + \int_{L_x} \mathbf{v}_b \cdot \mathbf{n}_2 \, dx + \int_{L_y} \mathbf{v}_r \cdot \mathbf{n}_2 \, dy
\tag{15}
$$

where $\mathbf{v}_*$ is the flow rate respective to top (*t*), bottom (*b*) and right (*r*) boundaries. $\mathbf{n}_1$ and $\mathbf{n}_2$ are the unit normal vectors along vertical and horizontal axes. Therefore, $\widetilde{k}_{xx}$ and $\widetilde{k}_{xy}$ can be computed. The fluxes are computed for other boundaries in a similar way. Then, $\widetilde{k}_{yy}$ and $\widetilde{k}_{yx}$ can be computed.

However, the fluxes are not identical at the two parallel boundaries for a fractured medium. To this end, we introduce the treatment proposed by Chen et al. (2008). Eq. (15) is evaluated twice respectively to left and right sides, denoted by $q_x^l$ and $q_x^r$. Consequently, $q_x = (q_x^l + q_x^r)/2$. The same treatment is applied on top and bottom sides, $q_y = (q_y^t + q_y^b)/2$.

The calculation of the upscaled permeability tensor is straightforward and derived from Darcy's law. Sometimes, the upscaled $\widetilde{\mathbf{K}}$ is asymmetric. The off-diagonal components are set to $(\widetilde{k}_{xy} + \widetilde{k}_{yx})/2$ as advised by Durlofsky (2005) and Chen et al. (2015).

For a two-phase flow, we refer to the works by Jackson et al. (2018) and Benham et al. (2021). The equivalent relative permeability is defined as:

$$
k_{r\alpha}(S_\alpha) = \frac{\langle u_\alpha \rangle \mu_\alpha L}{k_0 \langle \Delta p_\alpha \rangle}
\tag{16}
$$

where $\langle \cdot \rangle$ is a type of spatial averaging. $\Delta p_\alpha$ is the pressure drop between inlet and outlet. $L$ is the distance between inlet and outlet. $k_0$ is a typical dimensional scaling, which is selected as a mean permeability in practice. This expression is adapted from Jackson et al. (2018). Benham
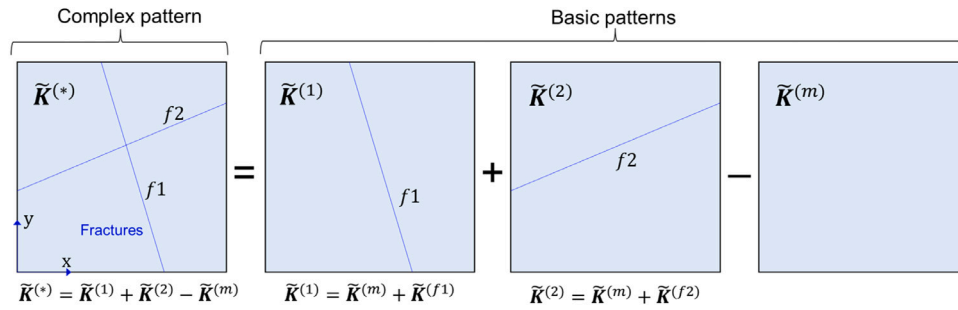
**Fig. 5.** An illustration of the superposition principle of equivalent permeability tensor.

et al. (2021) used it to upscale fluid flow in a porous medium. However, this formula is usually involved in analytical studies and inconvenient to implement.

Furthermore, it is worth noting that rigorously the relative permeability is a tensor $\mathbf{k}_{r\alpha}$ (Pickup and Serbie, 1996), which is absent in Eq. (16). In general, Darcy's law for multi-phase reads $\mathbf{u}_\alpha = -\mu_\alpha^{-1}\mathbf{k}_{r\alpha} \cdot \mathbf{K} \cdot (\nabla p)$. To do this, a result from Matthai and Nick (2009) is introduced in our work. They provided a method to upscale $\mathbf{k}_{r\alpha}$ according to the upscaled $\widetilde{\mathbf{K}}$. Here, we give the component forms, as shown in Appendix C.

### 4.2. Superposition principle of equivalent permeability tensor

A superposition principle of equivalent permeability tensor is integrated in this work for upscaling discontinuities. Assuming a matrix block intersected completely by several fractures, as shown in Fig. 5, each component of the equivalent tensor is equal to the summation contributed by these fractures respective to this component.

Alternatively, if we wish to calculate $\widetilde{\mathbf{K}}$ of a complex pattern, namely $\widetilde{\mathbf{K}}^*$, one can simply conduct a summation operation based on the known basic patterns. These basic patterns are constructed by single fracture cutting the porous rock with different geometrical parameters. As illustrated in Fig. 5, $\widetilde{\mathbf{K}}^{(1)}$ of a simple pattern consists of the contributions from the rock matrix and the single fracture, namely the superposition of them $\widetilde{\mathbf{K}}^{(1)} = \widetilde{\mathbf{K}}^{(m)} + \widetilde{\mathbf{K}}^{(f1)}$. Note that $\widetilde{\mathbf{K}}^{(m)}$ is obtained in the case without fractures. This idea can be extended to a more general case, where multi-fractures $n_f$ are considered:

$$\widetilde{\mathbf{K}}^{(*)} = \sum_i^{n_f} \widetilde{\mathbf{K}}^{(i)} - (n_f - 1)\widetilde{\mathbf{K}}^{(m)} \tag{17}$$

To show how it works, Fig. 5 provides an example when $n_f = 2$. An underlying assumption to this principle is that the interaction between fractures is neglected. It produces an acceptable error compared to the accurate solution. Note that this principle has been used in fractured reservoir simulation (Zhang et al., 1996; Lei et al., 2015; Xu and Yang, 2020). The validation of this principle will be elaborated through numerical tests in Section 5.

### 4.3. Treatment of complex configuration

The preceding content discusses the treatment to a dual fracture-pore medium, where the cavities are absent. For a fractured vuggy porous medium, the presence of cavities would impose significantly to hydraulic property of this medium (Huang et al., 2011; Golfier et al., 2015; Yan et al., 2019). In this section, the treatment of a complex pattern with the fracture-cavity networks is presented. Then, it will be employed in Section 5 for numerical study. It is worthwhile to note that the superposition principle proposed in Section 4.2 can be used in the upscaling procedure.

Fig. 6 shows a domain with complex geometry. It is partitioned using a physical decomposition (background grids), and then upscaled
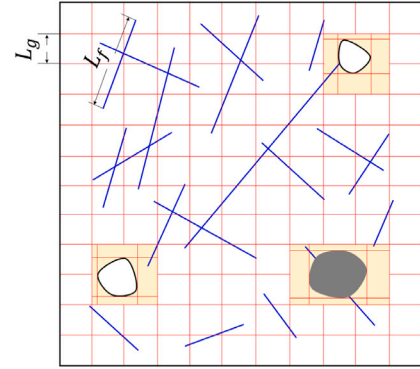


**Fig. 6.** Schematic of the domain with a complex geometry and the background grids.
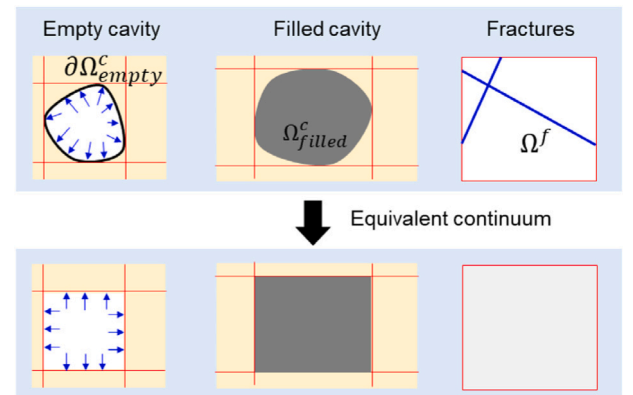


**Fig. 7.** Treatment of cavity and fractures in equivalent continuum.

by the flow-based equivalent continuum method. The pattern of physical decomposition is determined by the geometrical configuration, in which the distribution of cavities and fractures is an important factor.

The cavities with a periodic pattern are upscaled hydraulically as solid squares by Yan et al. (2019), which is reliable when the cavities are filled by geological materials. However, as discussed in Section 2.1 and Eq. (2), in some cases, a cavity can be treated as a region of constant pressure. In this case, the upscaling of cavity, which plays the role of an internal Dirichlet boundary, should be addressed, as shown in Fig. 7.

Consequently, this special situation is considered by imposing an internal pressure at the cavity walls. The cavities are upscaled as several sub-blocks for the convenience of meshing in the equivalent model and can reduces geometrical complexity. Each cavity covers several background grids, which consist of an influenced area as depicted in Fig. 6. We follow the notations defined in Section 2. Fig. 7 provides a novel treatment if a boundary condition $p = \bar{p}$ is imposed on edge $\partial\Omega_{empty}^c$.
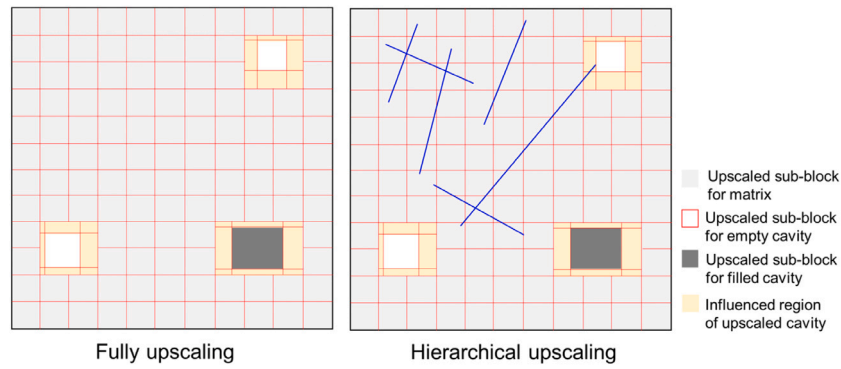
**Fig. 8.** Two different schemes regarding treatment of large size fractures.

Obviously, grid resolution $L_g$ has great impact on upscaling, as displayed in Fig. 6. In many remarkable works, the large size fractures are retained since they have influence on flow (Lee et al., 2001; Li and Lee, 2008). It is termed as "hierarchical upscaling" in this paper. Different size fractures are classified by a ratio $L_r = L_f/L_g$. Then, the upscaling procedure is performed based on different types of fracture, as illustrated in Fig. 8.

An alternative scheme is applied for the sake of convenient implementation (Chen et al., 2015; Yan et al., 2019; Azizmohammadi and Sedaghat, 2020). The matrix and all fractures are fully discretized by the background grids. It is termed as "fully upscaling" in this paper. Notably, Chen et al. (2015) upscaled the large size fractures by partitioning them into several sub-blocks which are intersected completely by fractures. Here, as displayed in Fig. 8, we present these two different treatments regarding the large size fractures.

## 5. Numerical tests and discussion

In this section, the proposed efficient implicit scheme and equivalent continuum approach are synthetically combined to simulate flow in fractured media. It should be noted that the capillary pressure is neglected for validation (Karimi-Fard et al., 2004; Moinfar et al., 2014; Jiang and Tchelepi, 2019). The superposition principle presented in Section 4.2 is integrated into the upscaling procedure. Then, fluid flow in a fractured medium with a complex geometry is studied using the approach introduced in Section 4.3. Note that the simulations are performed based on Intel Core i7-7950 processor at 2.6 GHz with 16 GB memory.

### 5.1. Numerical verification and convergence test

The benchmark is extracted from a publication by Karimi-Fard et al. (2004). Following the same setting in this literature, parameters of this model are set to porosity $\phi = 0.2$, permeability of matrix $k_m = 0.99 \times 10^{-15}\text{m}^2$ and fracture $k_f = 8.33 \times 10^{-10}\text{m}^2$, such that the fractures are modeled as a conductive channel. The coordinates of each fracture refer to Karimi-Fard et al. (2004).

The result simulated by DFM, as the reference solution, is used to compare the result computed by the proposed numerical scheme. Fluid is injected at the bottom left corner of the model, and the outlet is located at the top right corner, as shown in Fig. 9. This figure depicts several stages of saturation during evolution at different PVI (injected pore volume). Injection rate is 0.01 PVI/D. It appears that the result agrees well with the reference solution.

To test performance of the presented method under different conditions, we define a ratio, $k_r = k_f/k_m$, to measure the permeabilities of matrix and fractures. As reported in literature, the high contrast of permeability would induce an instability of simulators (Ţene et al., 2017). The ratio $k_r$ is set to $10^5$ and $10^{-5}$ to simulate two extreme situations. Note that $k_m = 1$ md. The former case describes fractures as

the conductive channels, while the later case represents the fractures as the barriers.

Because of the contrast of $k_f$ and $k_m$, the Jacobian becomes ill-conditioned, which is improved by the preconditioner **P** proposed in Section 3.2. Furthermore, the adaptive iterative scheme is applied to improve the convergence quality. Fig. 10 displays a set of curves to compare the grid convergence with different $k_r$. It shows that $k_r$ has great impact on the convergence performance. The convergence condition is gradually improved with a decreased $k_r$. Obviously, this test proves that the presented numerical scheme has a good convergence performance when the high contrast of permeability is involved.

Another test is performed to evaluate performance of the proposed adaptive iterative scheme in Section 3.2. To this end, computations by the improved scheme and classical scheme are carried out. The former scheme enjoys the advantage of adaptive iteration, while the later one uses a fixed time step during the entire iterative process. Fig. 11 shows a comparison of convergence performance during iteration using improved scheme and classical scheme with different $k_r$. Also, the total number of Newton iterations of both schemes is given. It appears that the presented method is able to improve the convergence condition and reduces the total time.

To study the grid convergence performance of this method, the model, as shown in Fig. 9, is simulated with different local grid refinements. The maximum and minimum values of the grid resolution are denoted by $h_{max}$ and $h_{min}$, respectively. Then, $h_{min}$ is allowed to be changed at a fixed $h_{max}$, as displayed in Fig. 12. The error $\epsilon_h$ is defined by the normalized difference between the reference solution and the results calculated using different local refinements. Fig. 13 provides the grid convergence with the refinement at a fixed $h_{max}$. It proves that the presented method has good performance of the grid convergence.

### 5.2. Study on superposition principle of equivalent tensor

In Section 4.2, the superposition principle is proposed for equivalent permeability tensor (EPT) based on the flow-based upscaling. Here, we analyze this principle using the presented numerical scheme. We use the dimensionless parameters. The size of the model is $1 \times 1$. The permeability of the fractures and matrix are $k_f = 10^5$ and $k_m = 1$. The inlet is placed on left boundary $p_L = 1$, while the outlet is placed on right boundary $p_R = 0$.

Fig. 5 provides an illustration of a fractured medium with a simple pattern. To study the superposition principle, EPT of several basic patterns should be calculated firstly, as displayed in Fig. 14, then a complex pattern can be easily obtained using these basic patterns. At this point, we use Eq. (17). Note that when $n_f > 2$, the superposition computation should be operated carefully. To explain it, Fig. 14 shows a case with $n_f = 3$, where the EPT of a complex pattern is calculated by $\widetilde{\mathbf{K}}^{(123)} = \sum_{i=1}^{3} \widetilde{\mathbf{K}}^{(i)} - 2 \times \widetilde{\mathbf{K}}^{(m)}$. It is worthwhile to notice that $\widetilde{\mathbf{K}}^{(m)}$ should be subtracted twice which equals to factor $(n_f - 1)$ in Eq. (17).

(a) Calculated by the presented method

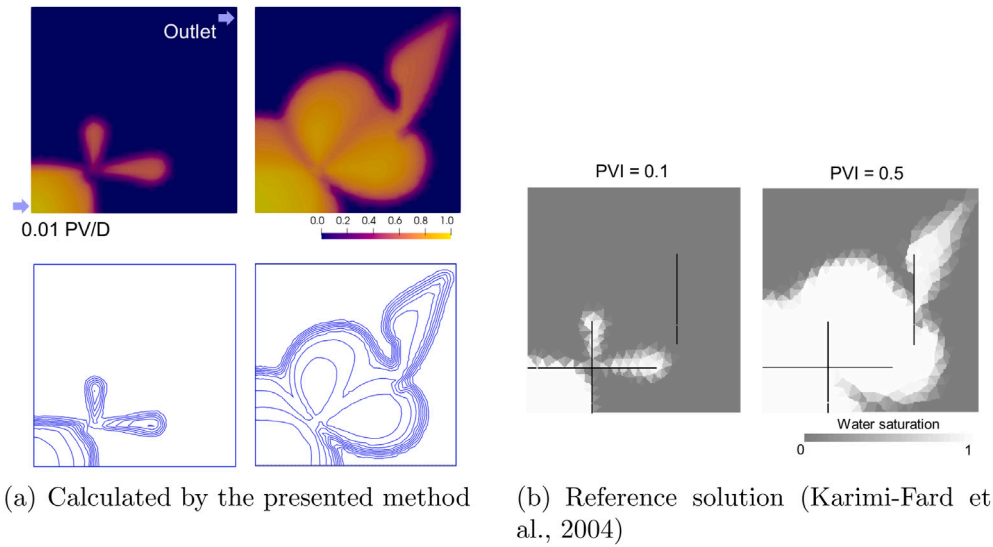(b) Reference solution (Karimi-Fard et al., 2004)

**Fig. 9.** Comparison of saturation evolution of the reference solution and the result calculated by the presented method at two different stages.
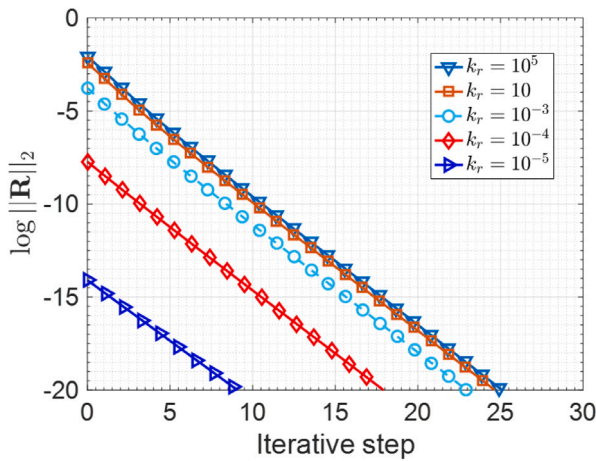


**Fig. 10.** Curves of convergence history with different $k_r$.

**Table 1**
Model parameters in simulation.

| Physical properties | Values | Units |
|---|---|---|
| Matrix permeability $k_m$ | $2 \times 10^{-12}$ | m$^2$ |
| Fracture permeability $k_f$ | $2 \times 10^{-17} \sim 2 \times 10^{-7}$ | m$^2$ |
| Fracture aperture $a^f$ | 0.1 | mm |
| Fracture porosity $\phi_f$ | 0.8 | – |
| Matrix porosity $\phi_m$ | 0.2 | – |
| Normalized saturation $S_n$ | $S_n = \frac{S_w - S_{wl}}{1 - S_{wl} - S_{nl}}$ | – |
| Relative permeabilities | Corey-type model | – |
| Exponent of Corey-type model $n_r$ | 2 | – |
| Capillary pressure $p_c$ | 0 | MPa |
| Irreducible saturation $S_{wl}$ | 0.001 | – |
| Irreducible saturation $S_{nl}$ | 0 | – |
| Dynamic viscosity of phase $w$ | 0.001 | Pa · s |
| Dynamic viscosity of phase $n$ | $5 \times 10^{-4}$ | Pa · s |

0.2, then the grid resolution $L_g$ is varied with the weight factor $\omega_{mesh}$. Then, $L_g = 0.05$ if $\omega_{mesh} = 4$, and $L_g = 0.1$ if $\omega_{mesh} = 2$. The inlet and outlet are $p_L = 1$ MPa and $p_R = 0$, on the left and right surfaces, respectively.

The physical properties of two-phase fluid are shown in Table 1. Note that the relative permeabilities follow the Corey-type model (Brooks and Corey, 1964):

$$k_{rw} = (S_n)^{n_r}, \quad k_{rn} = (1 - S_n)^{n_r} \quad (18)$$

where $n_r$ is the exponent of the Corey-type model. The normalized saturation $S_n$ is defined in Table 1.

An obvious difference between the DFM and upscaling approach is that the upscaled model might fail to describe the "sharp" discontinuous pressure jump around the fractures, as illustrated in the left hand side picture in Fig. 17. But their global distribution patterns agree well each other.

Fig. 16 shows the meshing strategy of different models. As shown in this figure, the unstructured grids are applied in the situation without upscaling (the DFM), where all fractures are retained and modeled explicitly. If upscaling is applied, these fractures are implicitly embedded inside the background grids by the equivalent continuum approach. The solid lines are explicitly modeled fractures, while the dashed lines are implicitly expressed.

The pressures distribution calculated by different models is displayed in Fig. 17. It demonstrates that the presence of fractures influences pressure field. A significant pressure gradient is observed around the fractures. It shows that the fully upscaling with different resolutions
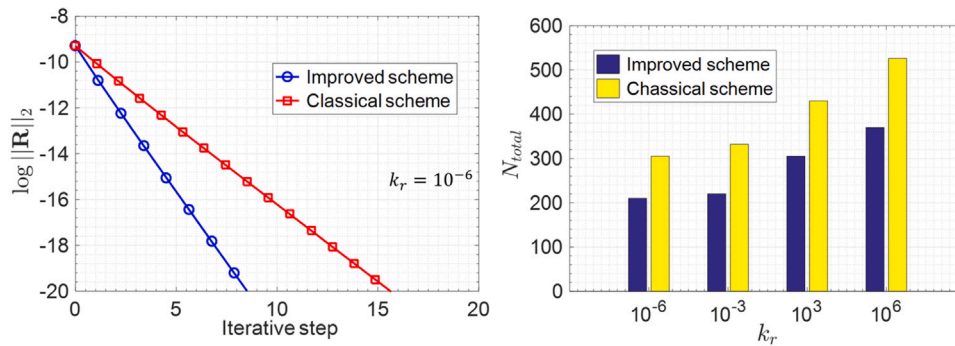
A comparison between results of the fluid flow simulation (FFS) and superposition principle (SP) is depicted in Fig. 14. The permeability tensors of the complex patterns are obtained from EPT of basic patterns. Error of each pattern is computed by $\sum \left\| \left( \widetilde{K}_{ij} - \hat{K}_{ij} \right) / \widetilde{K}_{ij} \right\|$, where the symbols $\hat{}$ and $\widetilde{}$ represent SP and FFS, respectively. It shows that the error is very small therefore the assumption of SP is validated in this test. The source of error is probably induced by the numerical discretization and grid resolution.

### 5.3. Flow in porous media with a fracture network

To demonstrate the performance of the proposed method, a porous medium with a fracture network is simulated. This fracture network contains different size fractures. The approach discussed in Section 4 is employed, as shown in Fig. 15.

The background grids with shade are the covered grids of fractures. Obviously, the resolution $L_g$ has great impact on the mesh pattern as well as the simulated results. In this stage, $L_g$ is determined by the fracture which has the smallest size. The smallest size is $L_{min}^f$, therefore $L_g = L_{min}^f / \omega_{mesh}$ with a weight factor $\omega_{mesh}$. Herein, we present two different $L_g$ to show the effect of grid resolution on mesh patterns and simulation results. As shown Fig. 15, the minimum length of fractures is

**Fig. 11.** Comparison of two different schemes with different $k_r$. Iteration in one time step (left) and the total number of Newton iterations $N_{total}$ (right).
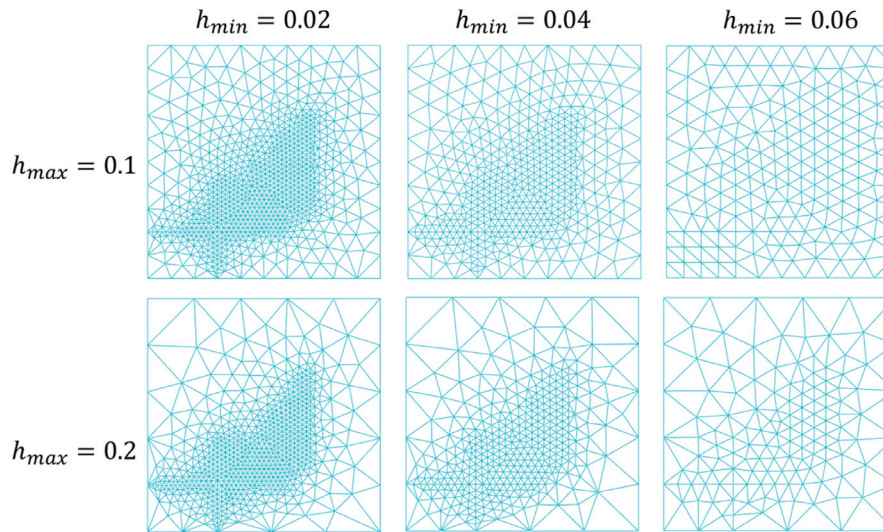


**Fig. 12.** Computational grids with different patterns of local refinement. $h_{max}$ and $h_{min}$ are the maximum and minimum resolutions, respectively.
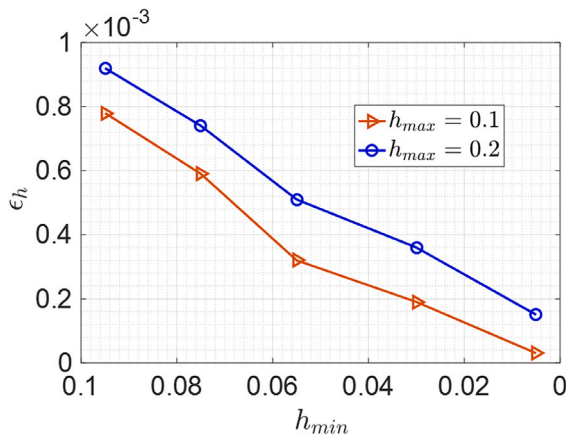


**Fig. 13.** Grid convergence performance with different resolutions corresponded to Fig. 12.

is able to reproduce this phenomenon. Note that the solution calculated by the hierarchical upscaling is very closed to that of the DFM.

To compare the results by different models, a survey line is placed along the off-diagonal crossing this domain. This line cuts several fractures through its path, as shown in Fig. 18. Although the curve calculated by upscaling with $L_g = 0.05$ has a slight oscillation, the global tendency agrees well with the curve of without upscaling. However, the accuracy is reduced if a coarse resolution (for example $L_g = 0.1$)

is employed. This test proves that the simulated result is obviously impacted by resolution, as pointed out in some studies (Karimi-Fard et al., 2004; Lee et al., 2001).

Computation using DFM is more accurate than using upscaling approach, but it needs to simulate all fractures explicitly and leads to an expensive cost. Compared to DFM, the advantage of the equivalent continuum model is the use of structured grids instead of unstructured grids, and the fractures are modeled implicitly, as displayed in Fig. 16. To show their difference in aspect of convergence performance, Fig. 18 provides a comparison of convergence history measured by $L^2$ norm of residual of these two different schemes. It explains that the upscaling approach improves the performance of convergence compared with the DFM.

Fig. 20 displays saturation evolution simulated by different models. To show the effect of fractures on hydraulic feature, a high contrast permeability ratio is set to $k_r = k_f/k_m = 10^{-5}$. It is observed that the fracture network plays a role of barrier to block fluid flow. Consequently, the fluid accumulates at top and bottom sides since the fractures block the movement. It shows that a fine resolution ($L_g = 0.05$ in this case) would lead to a more accurate result compared to a coarse resolution. Fig. 19 displays a set of curves of the cumulative production versus pore volume injection. The contrast of permeability between the fractures and the rock matrix is reflected by $k_r$, and it has significant influences on accuracy. The high conductivity of fractures would lead to a relative high production compared to the low conductivity.

| | $\widetilde{K}^{(m)}$ | $\widetilde{K}^{(1)}$ | $\widetilde{K}^{(2)}$ | $\widetilde{K}^{(3)}$ | $\widetilde{K}^{(4)}$ |
|---|---|---|---|---|---|
| Basic patterns | | $f1$ | $f2$ | $f3$ | $f4$ |
| Calculated by FFS | $\widetilde{K}^{(m)} = \begin{pmatrix} 1 & 10^{-3} \\ 10^{-3} & 1 \end{pmatrix}$ | $\widetilde{K}^{(1)} = \begin{pmatrix} 3.625 & 0.044 \\ 0.044 & 1.260 \end{pmatrix}$ | $\widetilde{K}^{(2)} = \begin{pmatrix} 3.651 & -0.067 \\ -0.067 & 1.279 \end{pmatrix}$ | $\widetilde{K}^{(3)} = \begin{pmatrix} 3.610 & -0.062 \\ -0.062 & 1.305 \end{pmatrix}$ | $\widetilde{K}^{(4)} = \begin{pmatrix} 2.765 & 2.629 \\ 2.515 & 2.765 \end{pmatrix}$ |
| | $\widetilde{K}^{(12)}$ | $\widetilde{K}^{(13)}$ | $\widetilde{K}^{(23)}$ | $\widetilde{K}^{(123)}$ | $\widetilde{K}^{(34)}$ |
| Complex patterns | $f1$  $f2$ | $f1$  $f3$ | $f2$  $f3$ | $f1$  $f2$  $f3$ | $f4$  $f3$ |
| Calculated by SP | $\hat{K}^{(12)} = \begin{pmatrix} 6.276 & -0.023 \\ -0.023 & 1.640 \end{pmatrix}$ | $\hat{K}^{(13)} = \begin{pmatrix} 6.224 & -0.019 \\ -0.019 & 1.565 \end{pmatrix}$ | $\hat{K}^{(23)} = \begin{pmatrix} 6.250 & -0.130 \\ -0.130 & 1.585 \end{pmatrix}$ | $\hat{K}^{(123)} = \begin{pmatrix} 8.875 & -0.086 \\ -0.086 & 1.844 \end{pmatrix}$ | $\hat{K}^{(34)} = \begin{pmatrix} 5.375 & 2.566 \\ 2.452 & 3.070 \end{pmatrix}$ |
| Calculated by FFS | $\widetilde{K}^{(12)} = \begin{pmatrix} 6.221 & -0.023 \\ -0.023 & 1.671 \end{pmatrix}$ | $\widetilde{K}^{(13)} = \begin{pmatrix} 6.197 & -0.020 \\ -0.020 & 1.578 \end{pmatrix}$ | $\widetilde{K}^{(23)} = \begin{pmatrix} 6.182 & -0.128 \\ -0.128 & 1.565 \end{pmatrix}$ | $\widetilde{K}^{(123)} = \begin{pmatrix} 8.592 & -0.082 \\ -0.082 & 2.142 \end{pmatrix}$ | $\widetilde{K}^{(34)} = \begin{pmatrix} 5.656 & 2.432 \\ 2.623 & 3.161 \end{pmatrix}$ |
| Error | 2.18% | 3.95% | 1.04% | 0.15% | 2.26% |
| Average error | | | 2.40% | | |

**Fig. 14.** Equivalent permeability tensors calculated by superposition principle (SP) and fluid flow simulation (FFS) and the corresponding errors.
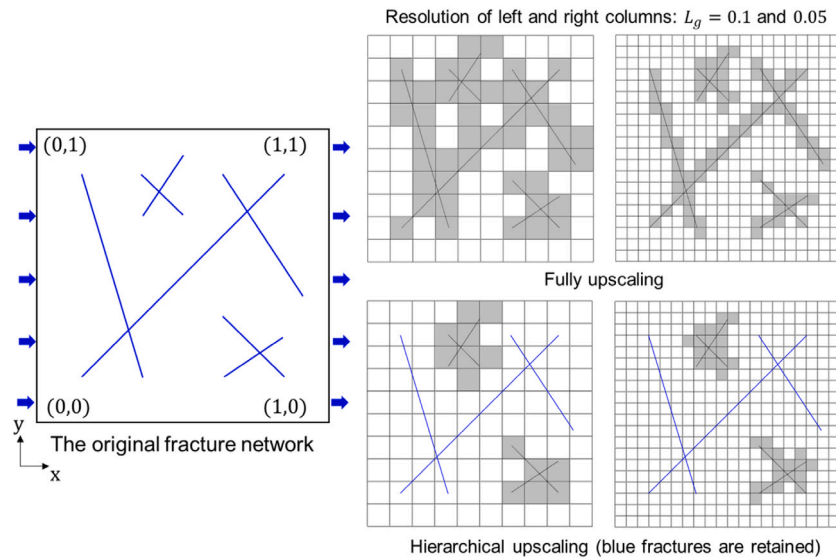


Resolution of left and right columns: $L_g = 0.1$ and $0.05$

(0,1)  (1,1)

(0,0)  (1,0)

The original fracture network

Fully upscaling

Hierarchical upscaling (blue fractures are retained)

**Fig. 15.** Fracture covered region of fully and hierarchical upscaling schemes for a fractured porous medium with different resolutions.



Unstructured grids for DFM

Structured grids with upscaling ($L_g = 0.05$)

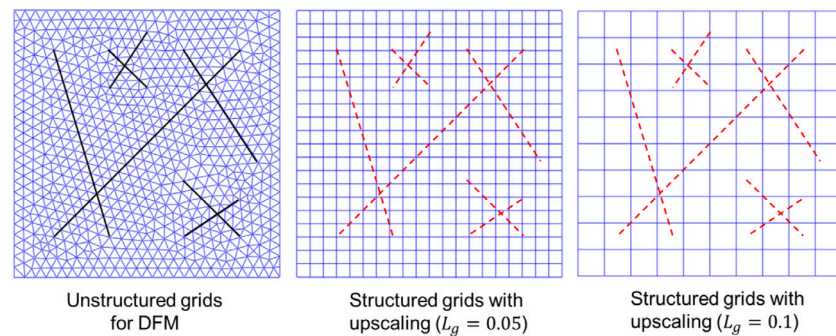Structured grids with upscaling ($L_g = 0.1$)

**Fig. 16.** Mesh strategies of the fracture networks for DFM and upscaling methods. The dashed lines are implicitly embedded.
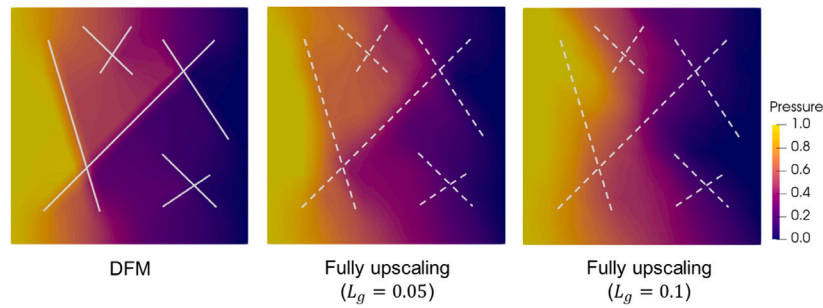
**Fig. 17.** Pressure distribution calculated by different strategies. A fine resolution produces a relative accurate result. The dashed lines are implicitly embedded.
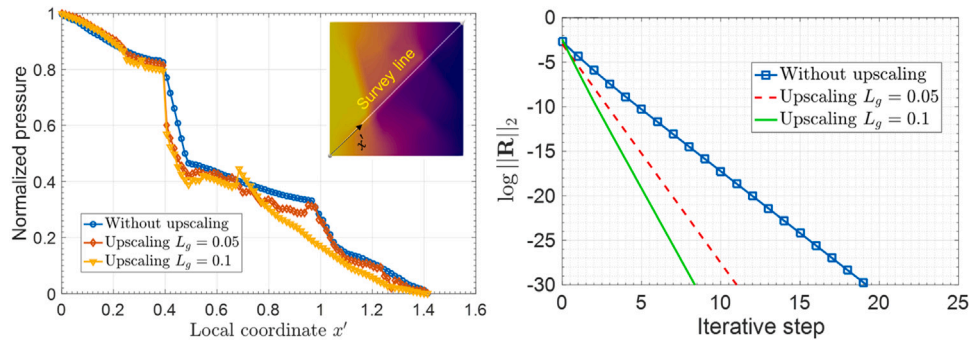


**Fig. 18.** Curves of pressure distribution along a survey line (left). The convergence history within one time step calculated by different strategies (right).
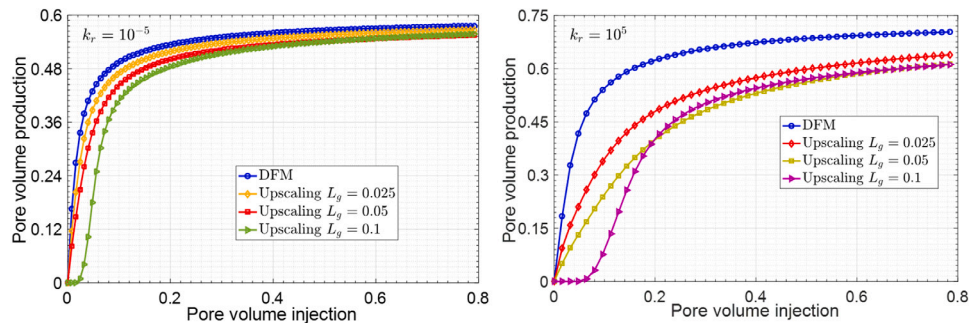


**Fig. 19.** Curves of the cumulative production versus pore volume injection using different models.

### 5.4. A complex geometry

A test is performed with a complex geometry to study fluid flow in a more complex porous medium. This model is the so-called fractured vuggy porous medium found in literature (Huang et al., 2011; Yan et al., 2019). An essential difference between a cavity and a fracture is the spatial extension. It results in different treatments of discretization for these two objects. We follow the scheme proposed in Section 4.3 to model the fractured media with complex geometry.

A fractured vuggy porous medium is shown in Fig. 21. The parameters are shown in Table 1. Note that the permeability of the filled cavity is set to $1 \times 10^{-13}\text{m}^2$. The dimensions in x- and y-axes are both 100 m. In this simulation, the filled and empty cavities are considered. It reproduces a typical situation in carbonate reservoir engineering (Huang et al., 2011; Wei et al., 2020; Wang et al., 2022), in which the connection of fractures and cavities constructs a connected channel system. The inlet condition is imposed on the edge of a cavity with pressure $p_{in} = 1$ MPa, while the outlet is placed on the edge of another cavity $p_{out} = -1$ MPa. These two cavities are connected by fracture networks. Two approaches, DFM (without-upscaling) and upscaling, are applied to simulate fluid flow. Thus, two different mesh

strategies are adapted, as shown in Fig. 21. The gray cells are embedded fracture-cavity zones, which need to be upscaled.

Fig. 22 provides saturation evolution of the porous medium as well as that of the fracture networks. Pressure distributions with respect to three different models are given in Fig. 23. It appears that discrete fracture model provides an accurate result but it requires explicitly simulation of all fractures. The upscaling approach depicts similar result and the accuracy is increased with a finer resolution ($L_g = 0.025$ is better than $L_g = 0.05$). A survey line is placed along the off-diagonal of the domain. Pressure variation along this line is displayed in Fig. 24.

Correspondingly, the relation of number of active grid cells versus pore volume injection is shown in Fig. 24. It demonstrates that the proposed equivalent continuum approach provides an efficient tool to model fluid flow in complex fractured media in a simple way. The results simulated by equivalent continuum approach are shown in Fig. 26.

Different resolutions lead to different computational steps. Fig. 25 provides a comparison analysis. Cell numbers of $L_g = 0.1$, 0.05, 0.025 and 0.0125 are 100, 400, 1600 and 6400, respectively. Correspondingly, we select cell number $n = 108$, 398, 1636 and 6423 for DFM on unstructured grids. It shows that the total number of Newton iterations $N_{total}$ of upscaling scheme is relatively smaller than that of DFM. The
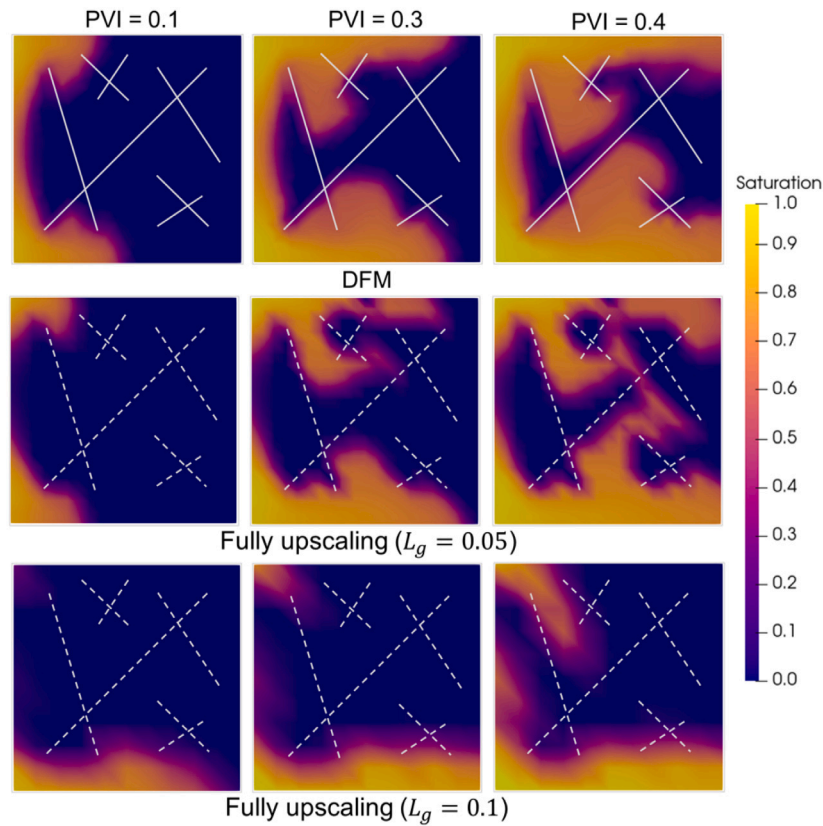
**Fig. 20.** Saturation evolution at different stages calculated by different models. The accurate of upscaling strongly depends on $L_g$. The dashed lines are implicitly embedded.
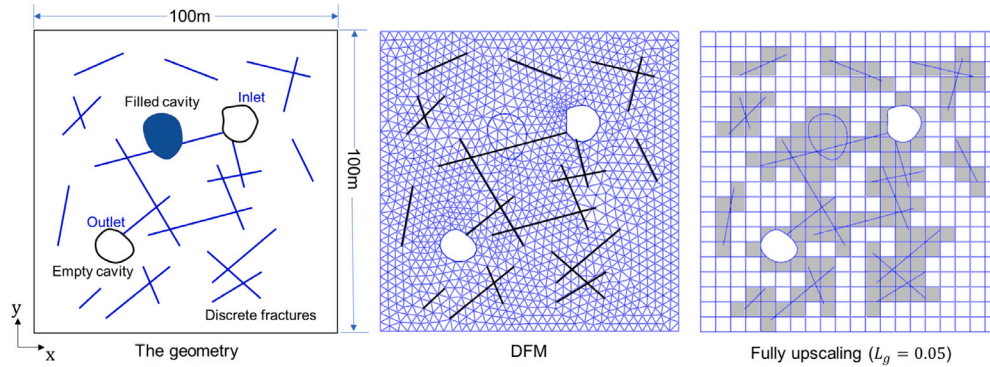


**Fig. 21.** Mesh of a fractured vuggy porous medium using different strategies.

adaptive time (AT) reduces the computation steps compared to fixed time (FT).

A test is analyzed with a more strict convergence criterion. The $L^2$ norm of residual is $10^{-15}$ and initial $\Delta t = 10^{-3}, 10^{-4}$. The adaptive iteration enforces the time step more smaller compared to the previous iterative step, as shown in Fig. 27. The error calculated by different resolutions $L_g$ is provided in this figure. It is measured by the relative difference between the solutions of DFM and upscaling model, $|S^{DFM} - S^{Up}|/S^{DFM}$. It shows that the error is relative small if a fine $L_g$ is applied. The maximum error calculated based on an extremely fine resolution (for example $L_g = 0.0125$) is 4.4%. However, it would produce an expensive computation cost, which is greater than 1000 Newton iteration number, as shown in Fig. 25. In contrast, if a more coarser grid resolution is applied (for example $L_g = 0.025$), the error is acceptable but the cost is highly reduced to around 600 iterations. It is more efficient than the finer grids. Thus, finding a balance between accuracy and computational cost is a key point in practice.

The relation of cumulative production versus injection is shown in Fig. 28. The inlet and outlet are both placed on cavities. It illustrates that the heterogeneity of permeability $k_r$ influences the production. In this case, the use of $L_g = 0.025$ in equivalent continuum model is sufficiently to recover the results of DFM.

## 6. Conclusions

In this work, an efficient implicit scheme with adaptive iteration is developed to simulate fluid flow in the fractured media with complex geometries. An equivalent continuum approach is devised and then integrated in the simulator combining with the superposition principle of equivalent permeability tensor. In the numerical scheme, a preconditioner is proposed to improve the condition of Jacobian, and an adaptive iterative strategy is used to improve the convergence performance. To model the fractured medium with a complex geometry, especially the fracture-vuggy network, we introduce a novel treatment
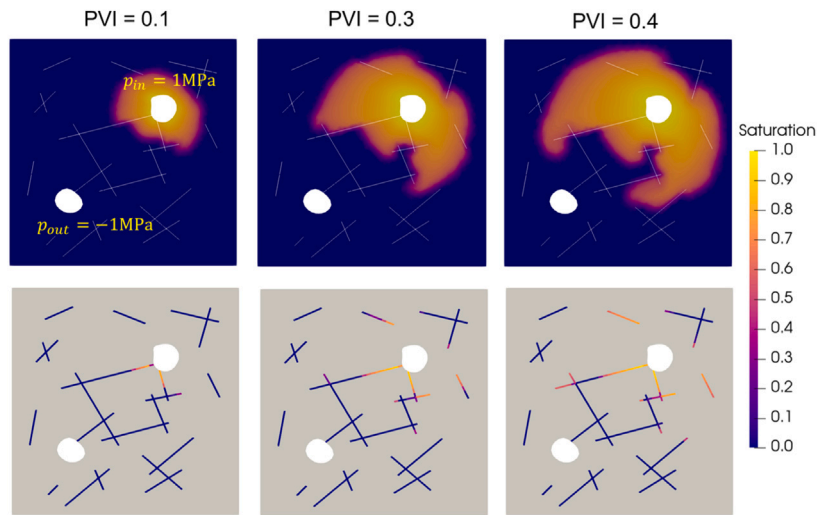
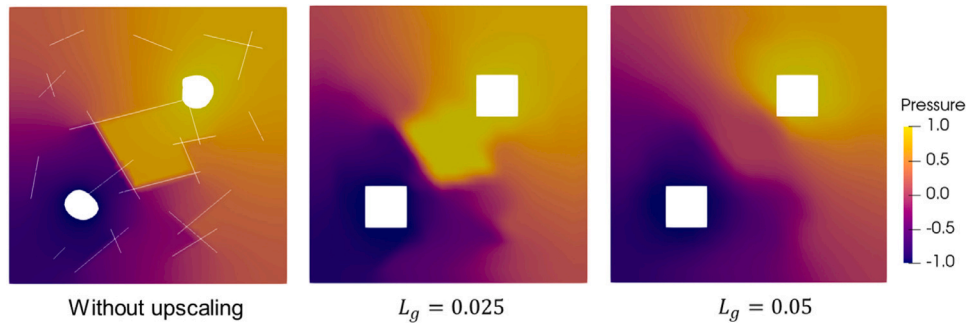**Fig. 22.** Saturation evolution in the rock matrix and fracture networks (DFM solution).



**Fig. 23.** Comparison of pressure distribution in different models.
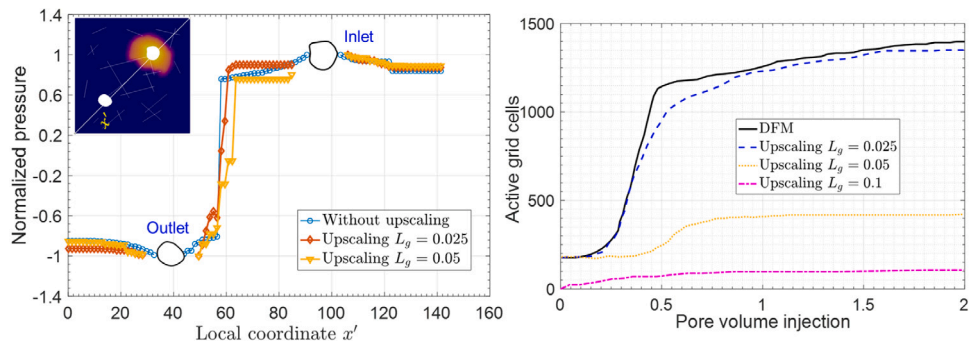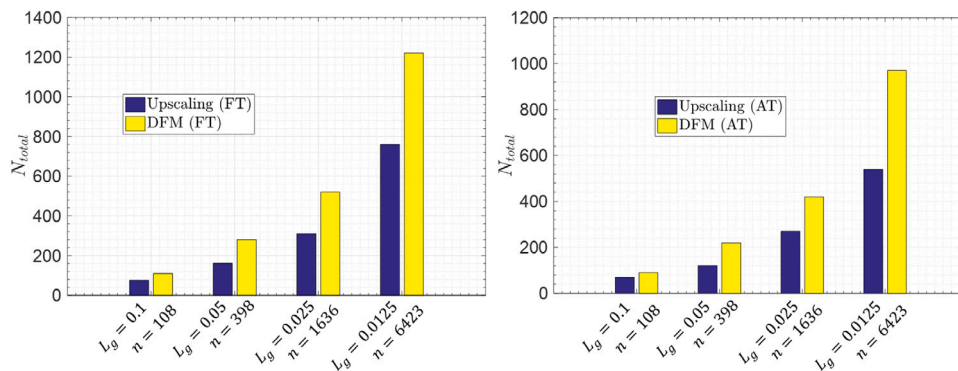


**Fig. 24.** Comparison of two different schemes. Pressure along a survey line (left). The number of active cells versus pore volume injection (right).



**Fig. 25.** Comparison of total number of Newton iterations using fixed time step (FT) and adaptive time step (AT). $n$ is the cell number of DFM, $L_g$ the resolutions of upscaling.
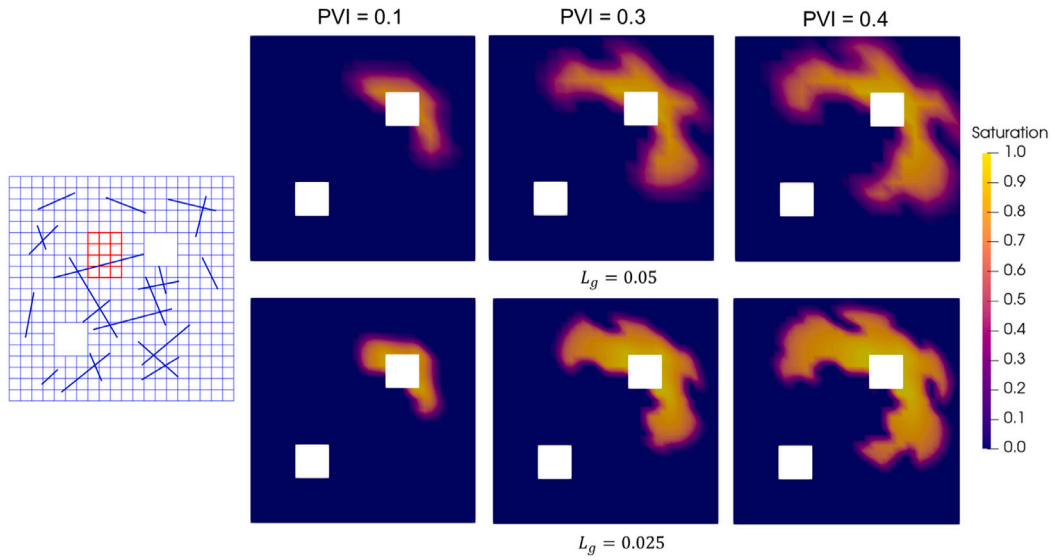
**Fig. 26.** Saturation evolution calculated by the equivalent continuum model with different resolutions. The grids ($L_g = 0.025$) shown in left side correspond to Fig. 21.
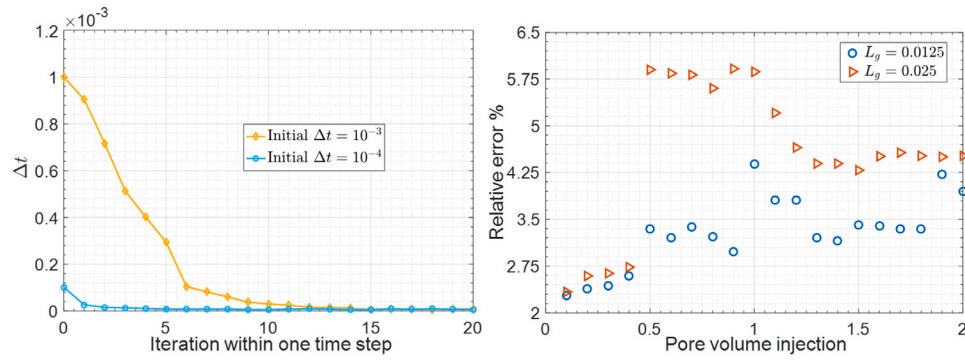


**Fig. 27.** Adaptive steps when a strict convergence criterion (threshold $10^{-15}$) is applied (left). Errors are calculated based on the cells placed at the off-diagonal along the domain (right).
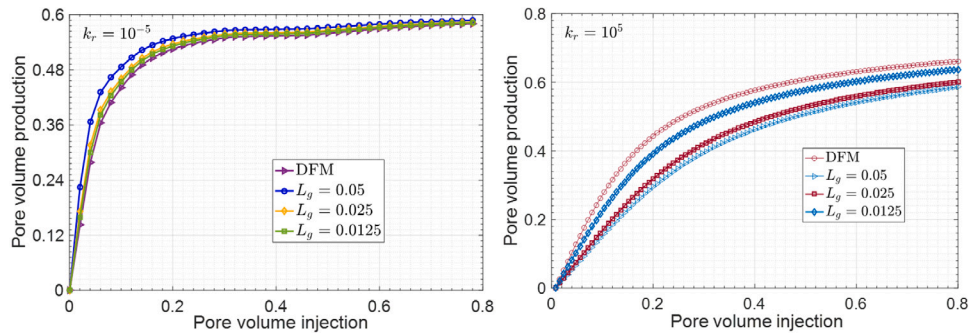


**Fig. 28.** Curves of the cumulative production versus volume pore injection of the fractured vuggy porous medium calculated by different models.

to upscale cavities, which allows a cavity either filled or empty. This scheme is able to simulate the inlet and outlet placed on the edge of cavity.

Numerical tests are performed to verify the presented numerical scheme and the equivalent approach. Validation and grid convergence performance are evaluated through a benchmark study, where different local grid refinements are considered. A comparison study is conducted to show the merits of adaptive iteration. To valid the feasibility of using superposition principle in upscaling, a set of tests is carried out to demonstrate it. Then, based on this, we simulate fluid flow in a fractured vuggy porous medium. Different modeling strategies are

employed to analyze and compare their performances. It appears that the proposed equivalent continuum approach is able to reproduce the results computed by the DFM. The accuracy depends on resolution of the background grids. This method enjoys a low computational cost and good convergence performance compared with the DFM using fully discretized fractures.

Several extensions of the presented approach deserve a further investigation. It can be applied to a more general case, such as two-phase flow in three-dimensional fractured vuggy porous media, to release the huge computational cost for the fully discretized fractures especially in field scale simulations.

## CRediT authorship contribution statement

**Luyu Wang:** Conceptualization, Methodology, Software, Funding acquisition, Writing – original draft. **Fabrice Golfier:** Funding acquisition, Writing – review & editing. **Anne-Julie Tinet:** Writing – review & editing. **Weizhong Chen:** Funding acquisition, Writing – review & editing. **Cornelis Vuik:** Methodology, Writing – review & editing.

## Declaration of competing interest

The authors declare that they have no known competing financial interests or personal relationships that could have appeared to influence the work reported in this paper.

## Acknowledgments

## Appendix A. Upwind scheme for cell to cell connections

An unified formulation of upwind scheme for different cells is applied. But there are several slight differences in matrix and fracture cells. Following the discussion in Section 3.2, for $\omega_i^m$ or $\omega_i^c$, as illustrated in Fig. A.29, the upwind term reads:

$$\int_{\omega_i^{mc}} \left[\nabla \cdot \mathbf{u}_\alpha\right]^{n+1} dV = \sum_{*=j,k,m,\ldots}^{n_i^{neig}} \left[f_\uparrow \mathbf{u}_{i*}\right]^{n+1} A_{i*} \tag{A.1}$$

where $*$ is the index of neighbors of element $\omega_i^{mc}$. The number of its neighbors is $n_i^{neig}$. $A_{i*}$ is the area of interface between elements $\omega_i^{mc}$ and $\omega_*^{mc}$, in which the velocity placed at this interface is $\mathbf{u}_{i*}$.

For $\omega_i^f$, it reads:

$$\int_{\omega_i^f} \left[\nabla \cdot \mathbf{u}_\alpha\right]^{n+1} dV = \sum_{*=j,k,m,\ldots}^{n_i^{neig}} \left[f_\uparrow \mathbf{u}_{i*}\right]^{n+1} Z_{i*} \tag{A.2}$$

When the flux connection is fracture–fracture, $Z_{i*} = a_i^f$; when it is matrix–fracture, $Z_{i*} = L_i^f$. All notations are defined in Section 3.2.

Both terms $\left[f_\uparrow \mathbf{u}_{i*}\right]$ in Eqs. (A.1) and (A.2) (also Eqs. (9) and (10)) are determined by the velocity direction or flux based on the so-called upwind scheme, as illustrated in Fig. A.29. For fracture elements:

$$\left[f_\uparrow \mathbf{u}_{i*}\right] = \begin{cases} \left[f_i \mathbf{u}_{i*}\right] & \text{if flux } \omega_i^f \to \omega_*^f \\ \left[f_* \mathbf{u}_{i*}\right] & \text{if flux } \omega_*^f \to \omega_i^f \end{cases} \tag{A.3}$$

It still validates for matrix and cavity elements.

## Appendix B. Formula of the preconditioner

As discussed in Section 3.2, the preconditioned Jacobian $\bar{\mathbf{J}}$ is derived by a preconditioner $\mathbf{P}$:

$$\bar{\mathbf{J}} = \mathbf{P}\mathbf{J} = \begin{bmatrix} \mathbf{A}^{-1} & \mathbf{0} & \mathbf{0} \\ \mathbf{0} & \mathbf{B}^{-1} & \mathbf{0} \\ \mathbf{0} & \mathbf{0} & \mathbf{C}^{-1} \end{bmatrix} \begin{bmatrix} \mathbf{J}^{mm} & \mathbf{J}^{mf} & \mathbf{J}^{mc} \\ \mathbf{J}^{fm} & \mathbf{J}^{ff} & \mathbf{J}^{fc} \\ \mathbf{J}^{cm} & \mathbf{J}^{cf} & \mathbf{J}^{cc} \end{bmatrix} \tag{B.1}$$

with the sub-matrices $\mathbf{A}$, $\mathbf{B}$ and $\mathbf{C}$. They are defined by the matrix norm of Jacobian. For convenience, we denote each row of $\mathbf{J}$ as sub-matrices $\mathbf{D}$, $\mathbf{E}$ and $\mathbf{F}$, such that $\mathbf{J} = [\mathbf{D} \ \mathbf{E} \ \mathbf{F}]^T$.
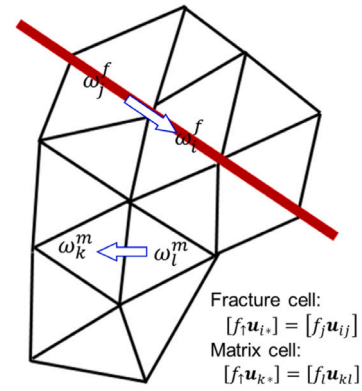


**Fig. A.29.** Illustration of the upwind scheme on unstructured grids.

The sub-block $\mathbf{A}$ in $\mathbf{P}$ is written as:

$$\mathbf{A} = \begin{bmatrix} \sqrt{\sum_{j=1}^{n_c^D}(D_{1j})^2} & \cdots & \cdots \\ \cdots & \sqrt{\sum_{j=1}^{n_c^D}(D_{2j})^2} & \cdots \\ \vdots & \ddots & \vdots \\ \cdots & \cdots & \sqrt{\sum_{j=1}^{n_c^D}(D_{n_r^D j})^2} \end{bmatrix} \tag{B.2}$$

with the numbers of columns $n_c^D$ and rows $n_r^D$ of $\mathbf{D}$. Similarly, $\mathbf{B}$ and $\mathbf{C}$ can be expanded following the same way. This preconditioner is easy to implement and flexible to integrate into a solver.

## Appendix C. Components of equivalent permeability tensor

Following the description and notations in Section 4.1, the components of permeability tensor are expressed by:

$$\widetilde{k}_{xx} = -\frac{\mu q_x L_x}{\Delta p L_y}, \ \widetilde{k}_{xy} = -\frac{\mu q_y L_x}{\Delta p L_x}$$
$$\widetilde{k}_{yy} = -\frac{\mu q_y L_y}{\Delta p L_x}, \ \widetilde{k}_{yx} = -\frac{\mu q_x L_y}{\Delta p L_y} \tag{C.1}$$

The components forms of relative permeability tensor are expressed by:

$$\widetilde{k}_{r\alpha,xx} = -\frac{\mu_\alpha q_{\alpha,x} L_x}{\widetilde{k}_{xx} \Delta p L_y}, \ \widetilde{k}_{r\alpha,xy} = -\frac{\mu_\alpha q_{\alpha,y} L_x}{\widetilde{k}_{xy} \Delta p L_x}$$
$$\widetilde{k}_{r\alpha,yy} = -\frac{\mu_\alpha q_{\alpha,y} L_y}{\widetilde{k}_{yy} \Delta p L_x}, \ \widetilde{k}_{r\alpha,yx} = -\frac{\mu_\alpha q_{\alpha,x} L_y}{\widetilde{k}_{yx} \Delta p L_y} \tag{C.2}$$

where $\Delta p$ is determined by boundary conditions. $L_x$ and $L_y$ are the width and height of the upscaled block. Other notations are defined in the preceding sections.

## References

Adeyemi, B., Ghanbarian, B., Winter, C.L., King, P.R., 2022. Determining effective permeability at reservoir scale: Application of critical path analysis. Adv. Water Resour. 159, 104096. http://dx.doi.org/10.1016/j.advwatres.2021.104096.

Adler, P.M., Thovert, J.F., Mourzenko, V.V., 2013. Fractured Porous Media. Oxford University Press, United Kingdom, http://dx.doi.org/10.1093/acprof:oso/9780199666515.001.0001.

Aliouache, M., Wang, X., Jourde, H., Huang, Z., Yao, J., 2019. Incipient karst formation in carbonate rocks: Influence of fracture network topology. J. Hydrol. 575, 824–837. http://dx.doi.org/10.1016/j.jhydrol.2019.05.082.

Aziz, K., 1979. Petroleum Reservoir Simulation. Applied Science Publishers, New York.

Azizmohammadi, S., Sedaghat, M., 2020. The impact of stress orientation and fracture roughness on the scale dependency of permeability in naturally fractured rocks. Adv. Water Resour. 103579. http://dx.doi.org/10.1016/j.advwatres.2020.103579.

Bahrainian, S.S., Dezfuli, A.Daneh., Noghrehabadi, A., 2015. Unstructured grid generation in porous domains for flow simulations with discrete-fracture network model. Transp. Porous Media 109, 693–709. http://dx.doi.org/10.1007/s11242-015-0544-3.

Benham, G.P., Bickle, M.J., Neufeld, J.A., 2021. Upscaling multiphase viscous-to-capillary transitions in heterogeneous porous media. J. Fluid Mech. 911 (A59), http://dx.doi.org/10.1017/jfm.2020.1134.

Berkowitz, B., 2002. Characterizing flow and transport in fractured geological media: A review. Adv. Water Resour. 25, 861–884. http://dx.doi.org/10.1016/S0309-1708(02)00042-8.

Brooks, R., Corey, A., 1964. Hydraulic Properties of Porous Media. Hydrol Pap, 3. Colorado State Univ, Fort Collins.

Chen, T., Clauser, C., Marquart, G., Willbrand, K., Mottaghy, D., 2015. A new upscaling method for fractured porous media. Adv. Water Resour. 80, 60–68. http://dx.doi.org/10.1016/j.advwatres.2015.03.009.

Chen, S.H., Feng, X.M., Isam, S., 2008. Numerical estimation of REV and permeability tensor for fractured rock masses by composite element method. Int. J. Numer. Anal. Methods Geomech. 32 (12), 1459–1477. http://dx.doi.org/10.1002/nag.679.

Cotta, R.M., Lisboa, K.M., Zotin, J.L.Z., 2020. Integral transforms for flow and transport in discrete and continuum models of fractured heterogeneous porous media. Adv. Water Resour. 142, 103621. http://dx.doi.org/10.1016/j.advwatres.2020.103621.

Țene, M., Bosma, S.B.M., Al Kobaisi, M.S., Hajibeygi, H., 2017. Projection-based embedded discrete fracture model (pEDFM). Adv. Water Resour. 105, 205–216. http://dx.doi.org/10.1016/j.advwatres.2017.05.009.

Durlofsky, L.J., 2005. Upscaling and gridding of fine scale geological models for flow simulation. In: 8th Int. Forum Reserv. Simul. Iles Borromees, Stresa, Italy.

Fourno, A., Ngo, T.D., Noetinger, B., Borderie, C.La., 2019. FraC: A new conforming mesh method for discrete fracture networks. J. Comput. Phys. 376, 713–732. http://dx.doi.org/10.1016/j.jcp.2018.10.005.

Gläser, D., Helmig, R., Flemisch, B., Class, H., 2017. A discrete fracture model for two-phase flow in fractured porous media. Adv. Water Resour. 110, 335–348. http://dx.doi.org/10.1016/j.advwatres.2017.10.031.

Golfier, F., Lasseux, D., Quintard, M., 2015. Investigation of the effective permeability of vuggy or fractured porous media from a Darcy-Brinkman approach. Comput. Geosci. 19, 63–78. http://dx.doi.org/10.1007/s10596-014-9448-5.

Hajibeygi, H., Olivares, M.B., HosseiniMehr, M., Pop, S., Wheeler, M., 2020. A benchmark study of the multiscale and homogenization methods for fully implicit multiphase flow simulations. Adv. Water Resour. 143, 103674. http://dx.doi.org/10.1016/j.advwatres.2020.103674.

Hosseini, M., Baghbanan, A., Seifabad, M.C., 2021. Using effective medium theory to calculate permeability of rock with complex fractures. Proc. Inst. Civ. Eng. Geotech. Eng http://dx.doi.org/10.1680/jgeen.21.00132.

Hoteit, H., Firoozabadi, A., 2008. An efficient numerical model for incompressible two-phase flow in fractured media. Adv. Water Resour 31 (6), 891–905. http://dx.doi.org/10.1016/j.advwatres.2008.02.004.

Huang, Z., Yao, J., Li, Y., Wang, C., Lv, X., 2011. Numerical calculation of equivalent permeability tensor for fractured vuggy porous media based on homogenization theory. Commun. Comput. Phys. 9 (1), 180–204. http://dx.doi.org/10.4208/cicp.150709.130410a.

Jackson, S.J., Agada, S., Reynolds, C.A., Krevor, S., 2018. Characterizing drainage multiphase flow in heterogeneous sandstones. Water Resour. Res. 54 (4), 3139–3161. http://dx.doi.org/10.1029/2017WR022282.

Jiang, J., Tchelepi, H.A., 2019. Nonlinear acceleration of sequential fully implicit (SFI) method for coupled flow and transport in porous media. Comput. Methods Appl. Mech. Engrg. 352, 246–275. http://dx.doi.org/10.1016/j.cma.2019.04.030.

Karimi-Fard, M., Durlofsky, L.J., Aziz, K., 2004. An efficient discrete-fracture model applicable for general-purpose reservoir simulators. SPE J. 9 (2), 227–236. http://dx.doi.org/10.2118/88812-PA.

Kolditz, O., Görke, U.J., Shao, H., Wang, W., 2012. Thermo-Hydro-Mechanical–Chemical Processes in Fractured Porous Media. Springer Science & Business Media.

Kottwitz, M.O., Popov, A.A., Abe, S., Kaus, B.J.P., 2021. Investigating the effects of intersection flow localization in equivalent-continuum-based upscaling of flow in discrete fracture networks. Solid Earth 12, 2235–2254. http://dx.doi.org/10.5194/se-12-2235-2021.

Lasseux, D., Valdés-Parada, F.J., Wood, B.D., 2021. Recent developments in upscaling and characterization of flow and transport in porous media. Adv. Water Resour. 150, 103886. http://dx.doi.org/10.1016/j.advwatres.2021.103886.

Lee, S.H., Lough, M.F., Jensen, C.L., 2001. Hierarchical modeling of flow in naturally fractured formations with multiple length scales. Water Resour. Res. 37, 443–455. http://dx.doi.org/10.1029/2000WR900340.

Lee, S., Mikeli, A., Wheeler, M.F., Wick, T., 2018. Phase-field modeling of two phase fluid filled fractures in a poroelastic medium. Multiscale Model. Simul. 16 (4), 1542–1580. http://dx.doi.org/10.1137/17M1145239.

Lei, G., Dong, P.C., Mo, S.Y., Yang, S., Wu, Z.S., Gai, S.H., 2015. Calculation of full permeability tensor for fractured anisotropic media. J. Pet. Explor. Prod. Technol. 5, 167–176. http://dx.doi.org/10.1007/s13202-014-0138-6.

Li, L., Lee, S.H., 2008. Efficient field-scale simulation of black oil in a naturally fractured reservoir through discrete fracture networks and homogenized media. SPE Reserv. Eval. Eng. 11 (4), 750–758. http://dx.doi.org/10.2118/103901.

Matthai, S.K., Nick, H.M., 2009. Upscaling two-phase flow in naturally fractured reservoirs. Am. Assoc. Pet. Geol. Bull. 93 (11), 1621–1632. http://dx.doi.org/10.1306/08030909085.

Medici, G., Smeraglia, L., Torabi, A., Botter, C., 2021. Review of modeling approaches to groundwater flow in deformed carbonate aquifers. Groundwater 59 (3), 334–351. http://dx.doi.org/10.1111/gwat.13069.

Mezhoud, S., Monchiet, V., Bornert, M., Grande, D., 2020. Computation of macroscopic permeability of doubly porous media with FFT based numerical homogenization method. Eur. J. Mech. B Fluids 83, 141–155. http://dx.doi.org/10.1016/j.euromechflu.2020.04.012.

Mohammed, I., Olayiwola, T.O., Alkathim, M., Awotunde, A.A., Alafnan, S.F., 2021. A review of pressure transient analysis in reservoirs with natural fractures, vugs and caves. Pet. Sci. 18, 154–172. http://dx.doi.org/10.1007/s12182-020-00505-2.

Moinfar, A., Varavei, A., Sepehrnoori, K., Johns, R.T., 2014. Development of an efficient embedded discrete fracture model for 3D compositional reservoir simulation in fractured reservoirs. SPE J. 19 (2), 298–303. http://dx.doi.org/10.2118/154246-PA.

Oda, M., 1985. Permeability tensor for discontinuous rock masses. Geotechnique 35 (4), 483–495. http://dx.doi.org/10.1680/geot.1985.35.4.483.

Pickup, G.E., Serbie, K.S., 1996. The scaleup of two-phase flow in porous media using phase permeability tensors. SPE J. 1 (4), 369–382. http://dx.doi.org/10.2118/28586-pa.

Ren, G., Jiang, J., Younis, R.M., 2018. A model for coupled geomechanics and multiphase flow in fractured porous media using embedded meshes. Adv. Water Resour. 112, 113–130. http://dx.doi.org/10.1016/j.advwatres.2018.09.017.

Schädle, P., Zulian, P., Vogler, D., Bhopalam, S.R., Nestola, M.G.C., Ebigbo, A., Krause, R., Saar, M.O., 2019. 3D non-conforming mesh model for flow in fractured porous media using Lagrange multipliers. Comput. Geosci. 132, 42–55. http://dx.doi.org/10.1016/j.cageo.2019.06.014.

Shewchuk, J.R., 2014. Reprint of: Delaunay refinement algorithms for triangular mesh generation. Comput. Geom. Theory Appl. 47, 741–778. http://dx.doi.org/10.1016/j.comgeo.2014.02.005.

Snow, D.T., 1969. Anisotropie permeability of fractured media. Water Resour. Res. 5 (6), 1273–1289. http://dx.doi.org/10.1029/WR005i006p01273.

Tan, X., Chen, W., Wang, L., Yang, J., Tan, X., 2021. Settlement behaviors investigation for underwater tunnel considering the impacts of fractured medium and water pressure. Mar. Georesources Geotechnol. 39 (6), 639–648. http://dx.doi.org/10.1080/1064119X.2020.1737279.

Wang, L., Chen, W., Tan, X., Tan, X., Yang, J., Yang, D., Zhang, X., 2020. Numerical investigation on the stability of deforming fractured rocks using discrete fracture networks: a case study of underground excavation. Bull. Eng. Geol. Environ. 79, 133–151. http://dx.doi.org/10.1007/s10064-019-01536-9.

Wang, L., Chen, W., Vuik, C., 2022. Hybrid-dimensional modeling for fluid flow in heterogeneous porous media using dual fracture-pore model with flux interaction of fracture-cavity network. J. Nat. Gas Sci. Eng. 104450. http://dx.doi.org/10.1016/j.jngse.2022.104450.

Wang, L., Chen, W., Yuan, J.Tan.X.Tan.X., Liu, Q., 2019. Evaluation of mountain slope stability considering the impact of geological interfaces using discrete fractures model. J. Mt. Sci. 16, 2184–2202. http://dx.doi.org/10.1007/s11629-019-5527-3.

Wei, S., Jin, Y., Xia, Y., 2020. Predict the mud loss in natural fractured vuggy reservoir using discrete fracture and discrete vug network model. J. Pet. Sci. Eng. 195, 107626. http://dx.doi.org/10.1016/j.petrol.2020.107626.

Xie, Y., Edwards, M.G., 2021. Higher resolution hybrid-upwind spectral finite-volume methods, for flow in porous and fractured media on unstructured grids. In: Society of Petroleum Engineers - SPE Reservoir Simulation Conference 2021. RSC 2021. -MS, http://dx.doi.org/10.2118/203957.

Xu, Z., Li, Z., Cui, S., Li, B., Chen, D., Zhang, Q., Zheng, L., Husein, M.M., 2022. Flow characteristics and EOR mechanism of foam flooding in fractured vuggy reservoirs. J. Pet. Sci. Eng. 211, 110170. http://dx.doi.org/10.1016/j.petrol.2022.110170.

Xu, Z., Yang, Y., 2020. The hybrid dimensional representation of permeability tensor: A reinterpretation of the discrete fracture model and its extension on nonconforming meshes. J. Comput. Phys. 415, 109523. http://dx.doi.org/10.1016/j.jcp.2020.109523.

Yan, X., Huang, Z., Yao, J., Zhang, Z., Liu, P., Li, Y., Fan, D., 2019. Numerical simulation of hydro-mechanical coupling in fractured vuggy porous media using the equivalent continuum model and embedded discrete fracture model. Adv. Water Resour. 126, 137–154. http://dx.doi.org/10.1016/j.advwatres.2019.02.013.

Yan, X., Sun, H., Huang, Z., Liu, L., Wang, P., Zhang, Q., Yao, J., 2021. Hierarchical modeling of hydromechanical coupling in fractured shale gas reservoirs with multiple porosity scales. Energy Fuels 35 (7), 5758–5776. http://dx.doi.org/10.1021/acs.energyfuels.0c03757.

Zhang, Q., Huang, Z., Yao, J., Wang, Y., Li, Y., 2017. Multiscale mimetic method for two-phase flow in fractured media using embedded discrete fracture model. Adv. Water Resour. 107, 180–190. http://dx.doi.org/10.1016/j.advwatres.2017.06.020.

Zhang, X., Sanderson, D.J., Harkness, R.M., Last, N.C., 1996. Evaluation of the 2-D permeability tensor for fractured rock masses. Int. J. Rock Mech. Min. Sci. Geomech. 33 (1), 17–37. http://dx.doi.org/10.1016/0148-9062(95)00042-9.